Ceramics International

Dielectric, Piezoelectric and Pyroelectric Properties of Ceramic Solid Solutions Based on PMN-PT and PZT

--Manuscript Draft--

Manuscript Number:	
Article Type:	Full length article
Keywords:	ferroelectrics; lead zirconate titanate; solid solutions; pyroelectric coefficients; dielectric properties; piezoelectric properties
Corresponding Author:	Aleksey Pavelko, Doctor of science Southern Federal University RUSSIAN FEDERATION
First Author:	Aleksey Pavelko, Doctor of science
Order of Authors:	Aleksey Pavelko, Doctor of science
	Alexander Martynenko
	Konstantin Andryushin
	Ekaterina Glazunova
	Alexandr Nagaenko
	Lidiya Shilkina
	Suleiman Kallaev
	Larisa Reznichenko
Abstract:	Using the method of two-stage solid-phase synthesis, involving mechanical activation of the synthesized powders and subsequent sintering using traditional ceramic technology, ferroelectric multicomponent solid solutions based on the PZT and PMN-PT systems were produced, characterized by fairly high Curie temperatures and pyroelectric coefficients, high coefficients of pyroelectric sensitivity and resistance to vibration interference, which makes it possible to classify them as to pyroelectric materials, are promising for use as working elements of sensors for pyroelectric receivers of radiant (thermal) energy.
Opposed Reviewers:	

Dielectric, Piezoelectric and Pyroelectric Properties of Ceramic Solid Solutions Based on PMN-PT and PZT

Aleksey Pavelko[1[0000-0002-1227-6990]], Alexander Martynenko[1[0009-0000-0424-8220]], Konstantin Andryushin[1[0000-0003-0147-8359]], Ekaterina Glazunova[1[0000-0002-2596-2471]], Alexander Nagaenko[1[0000-0003-3957-3941]], Lidiya Shilkina[1[0000-0002-8048-3617]], Suleiman Kallaev[2[0000-0002-2733-1833]], Larisa Reznichenko[1[0000-0003-4591-1601]]

[1]Southern Federal University, 344090 Rostov-on-Don, Russia
[2]Amirkhanov Institute of Physics DSC RAS, 367005 Makhachkala, Russia
aapavelko@sfedu.ru

Abstract. Using the method of two-stage solid-phase synthesis, involving mechanical activation of the synthesized powders and subsequent sintering using traditional ceramic technology, ferroelectric multicomponent solid solutions based on the PZT and PMN-PT systems were produced, characterized by fairly high Curie temperatures and pyroelectric coefficients, high coefficients of pyroelectric sensitivity and resistance to vibration interference, which makes it possible to classify them as to pyroelectric materials, are promising for use as working elements of sensors for pyroelectric receivers of radiant (thermal) energy.

Keywords: ferroelectrics, lead zirconate titanate, ceramics, solid solutions, phase transition, pyroelectric coefficients, dielectric properties, piezoelectric properties.

1 Introduction

The discovery and creation of new ferropiezoelectric materials with high pyroelectric properties, which can be used as working elements in pyroelectric radiant (thermal) energy detectors, is an important task in modern physical materials science. Pyroelectric detectors are used for remote temperature measurement of heated bodies, including moving ones (rolling mills, high-frequency furnaces for hardening or tempering steel, plastics production, food industry, etc.); for measuring heat flows (monitoring overheating of rubbing parts, etc.); and in security systems (fire protection, intrusion prevention). Pyroelectric detector sensors must be highly sensitive to weak thermal radiation over a sufficiently wide temperature range, mechanically robust, and stable over time. To achieve this, pyroelectric materials must possess a set of parameters, namely, maximum values of the pyroelectric coefficient γ and the complex coefficients $\gamma \times \varepsilon_0/(\varepsilon_{33}^T \times C_p)$ and γ/d_{31}. The former is proportional to the volt-watt sensitivity and, consequently, the detectability of the pyrodetector, while the latter characterizes the pyroelectric's resistance to vibration interference (a reduction in the piezoelectric modulus helps reduce the piezoelectric polarization that occurs on the pyroelectric electrodes under various influences).

Based on these parameters, the best pyroelectric materials, in most cases, are ferroelectrics (FEs), typically based on solid solutions of the PZT system. The wide range of possible applications of these materials is determined by their ability to form broad isomorphic phases by substituting the corresponding cations (Pb, Zr, and Ti), which improve their useful properties (ferroelectric, piezoelectric, pyroelectric, and others) [1-4]. For practical applications, ceramic materials based on the PZT system are optimized by modifying them with isovalent or heterovalent substitutions at the A- or B-positions of perovskite-type structures. Doping the PZT system makes it possible to control the electrophysical and piezoelectric parameters of ceramic samples, which allows for the production of materials with the desired functional properties [5-8]. Three-, four-, and five-component ceramic materials are constructed in this way [9-11]. It is known that the electrophysical properties of such ceramic materials depend significantly on the method of their production (technological process), that is, primarily, the methods of synthesis and sintering of the

materials. A promising basis for pyroelectric materials are multicomponent solid solutions based on the $PbZrO_3$-$PbTiO_3$ system [12-14], including relaxor components [15-18], such as $PbNb_{2/3}Zn_{1/3}O_3$-$PbTiO_3$ and $PbNb_{2/3}Mg_{1/3}O_3$-$PbTiO_3$. The present work is devoted to the development and study of the electrophysical and, first of all, pyroelectric properties of such multicomponent solid solutions.

2 Research Method

2.1 Materials and Research Methods

The objects of study were ceramic samples of solid solutions based on the $PbZrO_3$-$PbTiO_3$ (PZT) system: $PbTiO_3$-$PbZrO_3$-$PbNb_{2/3}Zn_{1/3}O_3$-$PbNb_{2/3}Mg_{1/3}O_3$ + MnO_2 (SS1) and $PbTiO_3$-$PbZrO_3$-$PbW_{1/2}Mn_{1/2}O_3$-$PbNb_{2/3}Mn_{1/3}O_3$ (SS2). The production of solid solutions was carried out by two-stage solid-phase synthesis followed by sintering using conventional ceramic technology. The selection of optimal technological modes was carried out on a series of experimental samples with x-ray control of the phase composition and relative density ($\rho_{rel.}$) of the samples. The optimal synthesis modes were T_{sint1} = 820 °C, T_{sint2} = 850 °C, τ_{sint1} = τ_{sint2} = 5 hours. Mechanical activation (MA) of the synthesized solid solution powders was carried out at the stage of manufacturing press powders prepared for sintering. MA was carried out in a high-energy grinding planetary ball mill AGO-2 (Russia). Grinding was carried out in an alcohol medium for 15 minutes, the drum rotation speed was 1820 rpm. Optimal sintering mode: $T_{sp.}$ = 1150 °C, sintering time $\tau_{sp.}$ = 3 hours. Search measurement samples were made in the form of disks with a diameter of 12 mm and a thickness of 1 mm. The electrodes were applied by burning silver-containing paste twice.

X-ray structural studies were carried out by powder diffraction on a DRON-3 diffractometer using CoKα radiation. The cell parameters were calculated using the standard method [26], the error in measuring the parameters was: $\Delta a = \Delta b = \Delta c = \pm 0.003$ Å, $\Delta V = \pm 0.05$ Å^3, where a, b, c are the cell parameters, V is the cell volume.

Experimental density of samples $\rho_{exp.}$ measured by hydrostatic weighing in octane. X-ray density was calculated using the formula: $\rho_{x\text{-}ray} = 1.66 \times M/V$, where M is the molecular weight per cell, V is the cell volume. The relative density was determined using the formula: $\rho_{rel.} = (\rho_{exp.}/\rho_{x\text{-}ray}) \times 100\%$.

To study the microstructure of the samples, a JSM-6390L scanning electron microscope (Japan) with a microanalyzer system from Oxford Instruments (UK) was used. The resolution of the microscope was 1.2 nm at an accelerating voltage of 30 kV (image in secondary electrons), the accelerating voltage range was from 0.5 to 30 kV, the magnification was from ×10 to ×1000000, and the beam current was up to 200 nA.

Specific heat (C_p) of the samples was measured by means of the differential scanning calorimeter DSC-204 F1 (NEZSCH).

The polarization of the samples was carried out in a chamber with polyethylene siloxane liquid at ~ 140 °C. Heating to the specified temperature was carried out according to a linear law for 0.5 h, accompanied by an increase in the constant electric field from 0 to 3 kV/mm. The samples were kept under these conditions for 25 minutes, after which they were cooled under the field to room temperature.

The dielectric, piezoelectric and pyroelectric properties of the obtained samples were studied in a wide temperature range. The study of relative dielectric constant ($\varepsilon/\varepsilon_0$) and dielectric losses (tgδ) was carried out in the temperature ranges T = 20...350 °C and measuring signal frequencies f = 20...10^6 Hz on a specially designed stand, including a high-temperature furnace, an SRS PTC10

thermal controller with a sensor temperature PT-100, as well as an LCR meter Agilent E4980A. Piezoelectric characteristics were measured automatically on the same bench using a Keysight E4990A impedance meter; the resonance-antiresonance method was used to calculate the piezoelectric parameters [27]. The relative dielectric constant of polarized samples ($\varepsilon_{33}^T/\varepsilon_0$), piezoelectric modulus ($|d_{31}|$), piezoelectric coefficient (piezosensitivity) ($|g_{31}|$), electromechanical coupling coefficient of planar vibration modes (K_p), mechanical quality factor (Q_M), Young's modulus (Y_{11}^E) were calculated and speed of sound (V_1^E). The errors in measuring electrophysical parameters have the following values: $\varepsilon_{33}^T/\varepsilon_0 \leq \pm$ 1.5%, $K_p \leq \pm$ 2.0%, $|d_{31}| \leq \pm$ 4.0%, $Q_M = \leq \pm$ 12%; $Y_{11}^E \leq \pm 0.7\%$. The piezoelectric modulus d_{33} was determined in the quasi-static mode on samples in the form of a disk using d33 meter YE2730A.

To study the pyroresponse, various methods were used: the quasi-static method, the temperature wave method and the radiation method [28].

To study the pyroelectric effect using the quasi-static method, we used the stand described above, in which, using an Agilent 4339B high-resistance meter, we measured the current i_{QS} flowing through a pyroelectric sample with a continuous change in its temperature at a rate of b = 1 °C/min, from which the pyroelectric coefficient was determined as $p_{QS} = i_{QS}/(Ab)$, where A is the surface area of the sample. The disadvantage of this method is the inability to separate currents of a pyroelectric nature from thermally stimulated currents that arise when the temperature of crystals with defects increases. To solve this problem, dynamic methods are used, one of which is the temperature wave method [29,30]. The method is based on the fundamental difference in the temperature behavior of pyroelectric (i_p) and thermally stimulated (i_{TS}) currents: i_p is reversible, and its value is proportional to the rate of temperature change – $i_p = pAb$, while i_{TS} within small temperature intervals is proportional to the temperature itself – $i_{TS} = i_0 + RT$, where R is a constant coefficient.

In our case, in a specially designed temperature chamber using an SRS PTC10 thermal controller, a sinusoidal temperature wave was set according to the law:

$$T = T_0 + T_1\sin(\omega t), \quad (1)$$

in this case, the wave amplitude T_1 was set in the range from 0.25 to 0.5 °C, and the average temperature T_0 was selected from the range 30...200 °C. In parallel, also using an Agilent 4339B high-resistance meter, the i_{HW} current generated by the sample was measured, which can be written as follows:

$$i_{HW} = i_0 + RT_0 + RT_1\sin(\omega t) + p_{HW}AT_1\omega\cos(\omega t).$$

It can be seen that the total current contains a non-pyroelectric contribution, in-phase with the temperature wave, and a pyroelectric component, leading the temperature wave by 90°. The sum of these oscillations gives the resulting current wave, directly measured in experiment, which can be represented in the following form:

$$i_{HW} = i_{dc} + i_1\sin(\omega t + \phi), \quad (2)$$

where $i_{dc} = i_0 + RT_0$, $i_1 = (i_p^2 + i_n^2)^{1/2}$, $i_p = p_{HW}AT_1\omega = i_1\sin(\phi)$, $i_n = RT_1 = i_1\cos(\phi)$.

If the recorded current is of a purely pyroelectric nature, $R = 0$ and $\phi = \pi/2$. If the sample generates both pyroelectric and non-pyroelectric currents, $R \neq 0$ and $\phi < \pi/2$. By dividing the measured current into two components in this way, it is possible to determine the value of the desired pyroelectric coefficient p_{HW}.

We also used the radiation dynamic method, first described by Chynoweth [31]. In this method, the surface temperature of the sample was continuously varied by a small amount around the average temperature by illuminating the sample with a sinusoidally varying flux of infrared radiation, while the average temperature varied continuously in the range from 20 to 240°C. As a result of this temperature change, the sample generated a pyroelectric current, the *rms* value of which was measured using an SR830 lock-in amplifier (Stanford Research Systems). This method

has many disadvantages, among which the main one is the difficulty of determining the absolute value of the pyroelectric coefficient p_{IR}, caused by the need for independent measurements of the heat capacity and thermal conductivity of the sample, the density of the incident radiation flux, and the absorption capacity of the irradiated electrode, due to which one cannot be sure of the actual temperature change in the sample. However, the great advantage of the method is that the described temperature change mode is close to the operating mode of pyroelectric detectors, which is of great importance from the point of view of the potential practical application of the materials under study. Due to these features, in this work p_{IR} is given in relative units.

3 Results

Figure 1 shows X-ray diffraction patterns of materials SS1 and SS2, obtained under different conditions, in the angle range 2θ = (20...80) degrees, as well as individual reflections 111 and 200 on an enlarged scale. X-ray phase analysis of the samples, the results of which are given in Table 1, showed that all solid solutions have a perovskite structure and there are no impurity phases. The symmetry of the crystal lattice of both materials is rhombohedral (Rh), since they are based on the solid solutions of the PZT system from the Rh region of its phase diagram. The X-ray lines in the X-ray diffraction pattern of the SS1 material are double, which indicates that the solid solution is inhomogeneous and consists of two solid solutions with similar cell parameters.

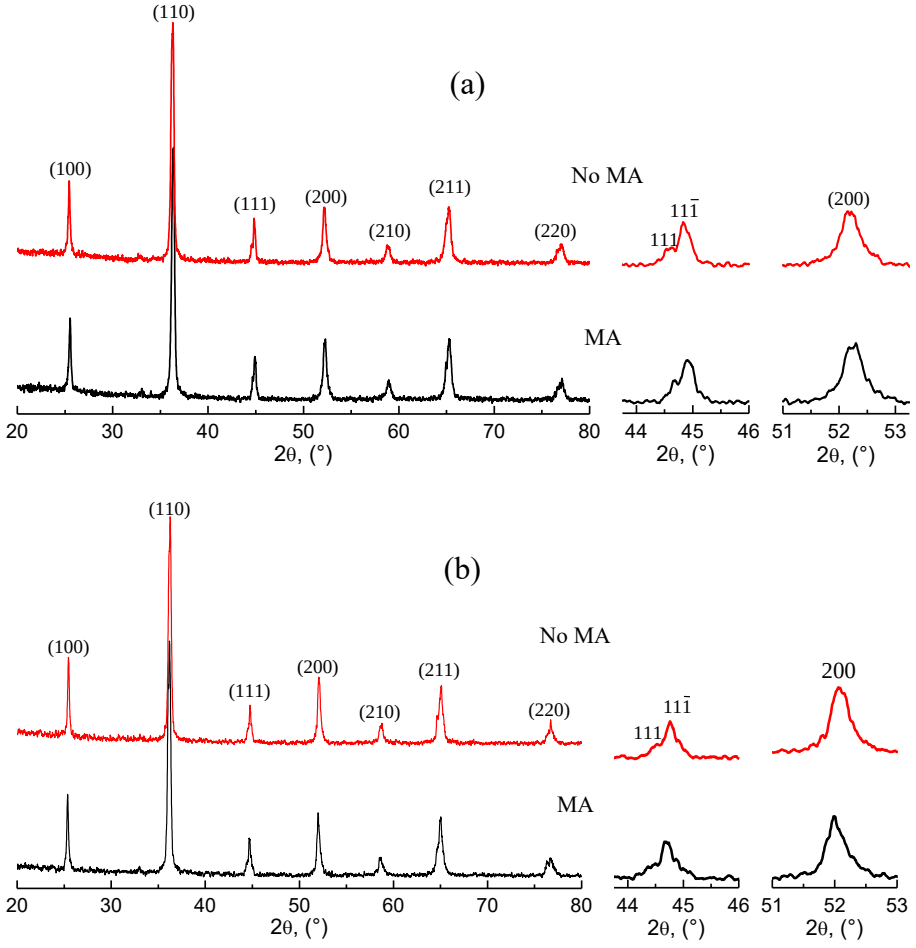

Fig. 1. X-ray diffraction patterns of materials SS1 (a) and SS2 (b), obtained using different conditions.

Typical images of the microstructure of ceramics obtained for various compositions at different magnifications are presented in Figure 2.

The grain landscape is determined by the following indicators: phasing of the crystal structure, porosity, presence and nature of the defects. Features of the phase structure are reflected in such elements of the grain structure as:

- average grain size;
- type of grain size distribution;
- nature and degree of uniform grain size (heterogeneity);
- the shape of the grains and the degree of its perfection;
- type of packaging (dense/loose, mosaic, chaotic, combined, block, radial-ring, with aggregation elements, etc.), presence and nature of texture.

Table 1. Structural parameters and densities of the obtained materials.

Material	Sintering mode	Phase	Symmetry	*a,* Å	α, (°)	*V*, Å^3	ρ_{exp}, g/cm^2	$\rho_{x\text{-}ray}$, g/cm^2	$\rho_{rel.}$, %
SS1	MA T_{sint}=1150 °C, 3 h.	100 Perovskite 2.5 ZrO_2	Rh	4.075	89.78	67.66	6.82	8.08	84.40
	No MA T_{sint}=1150 °C, 1.5 h.	100 Perovskite traces of ZrO_2	Rh	4.079	89.75	67.89	6.01	8.05	74.63
SS2	MA T_{sint}=1150 °C, 3 h.	100 Perovskite 2 ZrO_2	Rh	4.093	89.82	68.56	7.57	8.08	93.64
	No MA T_{sint}=1150 °C, 3 h.	100 Perovskite traces of ZrO_2	Rh	4.087	89.79	68.28	6.98	8.11	86.07

When describing porosity, the types of pores (open, closed, intergranular, intragranular), their average size, dispersion (range of size changes), dispersion (fineness), shape, nature of distribution, origin (technological, secondary, etc.) are analyzed.

Defectiveness is determined by the localization of cracks: transgranular, i.e. along the grain body, intercrystalline, inclusions of various natures, etc.

Following the above scheme for describing the grain structure of ferroelectric ceramics, let us consider the given fragments of the microstructures of the studied materials SS1 and SS2. Belonging to the group of ferroelectric-hard materials, these materials have a fine-grained (with an average grain size, $D_{av.}$, ~ 4...6 μm), densely packed, mosaic-chaotic, uniform-grained structure. The grains in SS1 are of irregular shape, and in SS2 they are close to the correct geometric shape.

A feature of the grain landscape of SS1 is the formation of areas with merged grains, between which pores are noticeable, most likely of artificial origin – “breakouts” formed during the mechanical processing of samples, which indicates a reduced strength of the boundaries of such

formations. In addition, attention is drawn to the fact of the presence of areas with the smallest unformed grains on the grain field, which most likely indicates local fluctuations in composition caused by the same local violations of the "average" technological regulations.

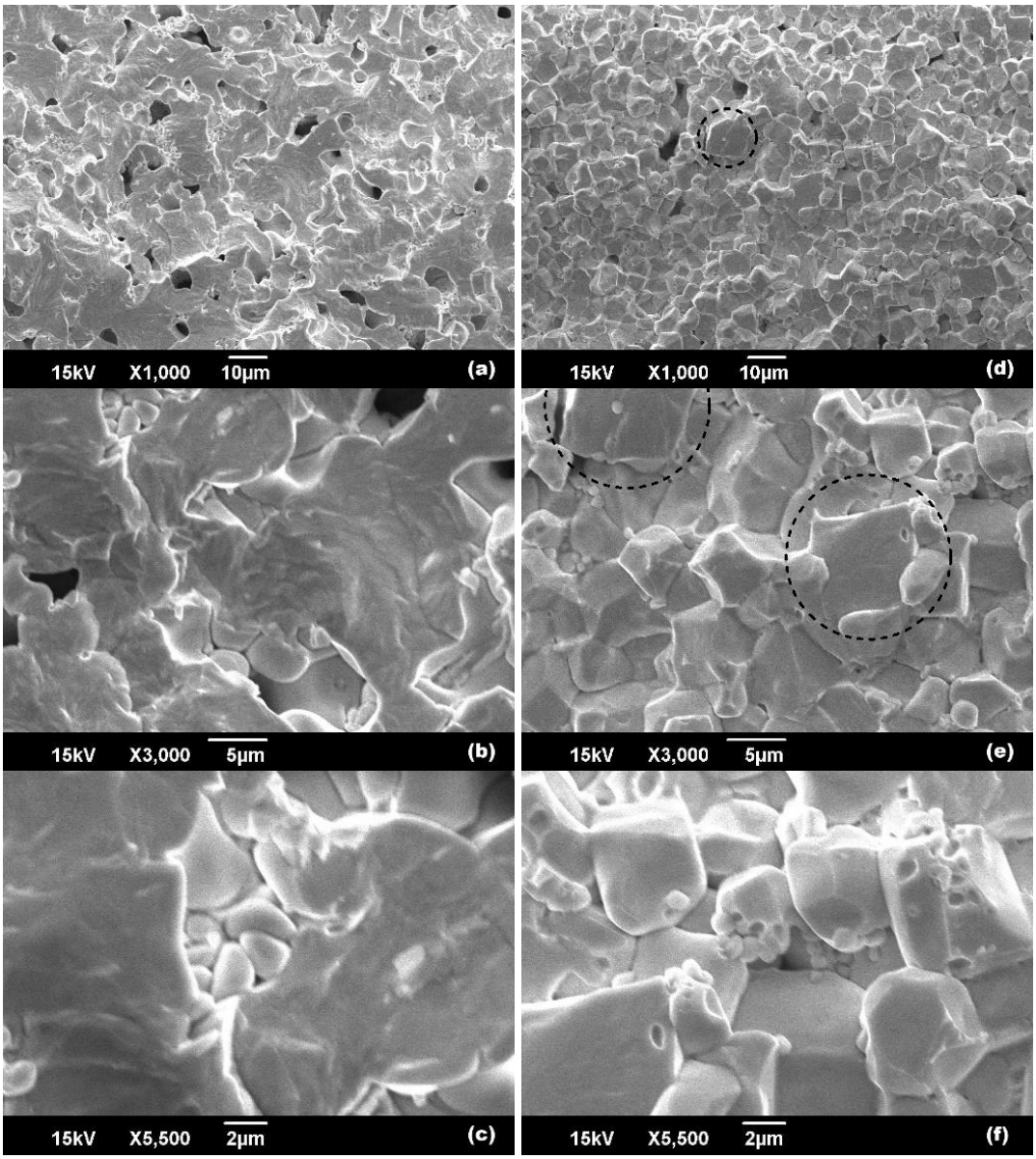

Fig. 2. Photographs of the microstructure of ceramic samples SS1 (a, b, c) and SS2 (d, e, f).

Characteristic of SS2 is the presence on the grain field of larger ($D_{av.}$ ~ 10...15 μm) grains with straight boundaries (see dashed lines in Figures 2 d, e). Most often, such ideomorphic grains are characteristic of processes of secondary discontinuous recrystallization, when impurities located at the grain boundary at the temperature of recrystallization sintering form a liquid phase that actively interacts with the base material, acting not so much as a “bundle” but as a transport medium, that is, a solvent. The selective growth of large grains in this case occurs due to ordinary dissolution and precipitation from solution, and not to movement of boundaries. In this case, the liquid covering the surface of such grains with a film causes them to acquire a certain growth form and regular cut, identical to the habit of crystals growing from a molten solution. As a result,

ideomorphic grains crystallize in the form of polyhedra with almost straight boundaries. Most often, such grains are surrounded by small grains that "parasitize" at their boundaries (Figure 2 f).

Sources of liquid phases can be Mn(IV) oxides with a melting point $T_{melt.}$ = 540°C and Mn(III) with $T_{mel.}$ = 1080°C, located in the charge of the SS2 material due to redox reactions occurring during the technological processing of the material, the elemental composition of which contains manganese ions.

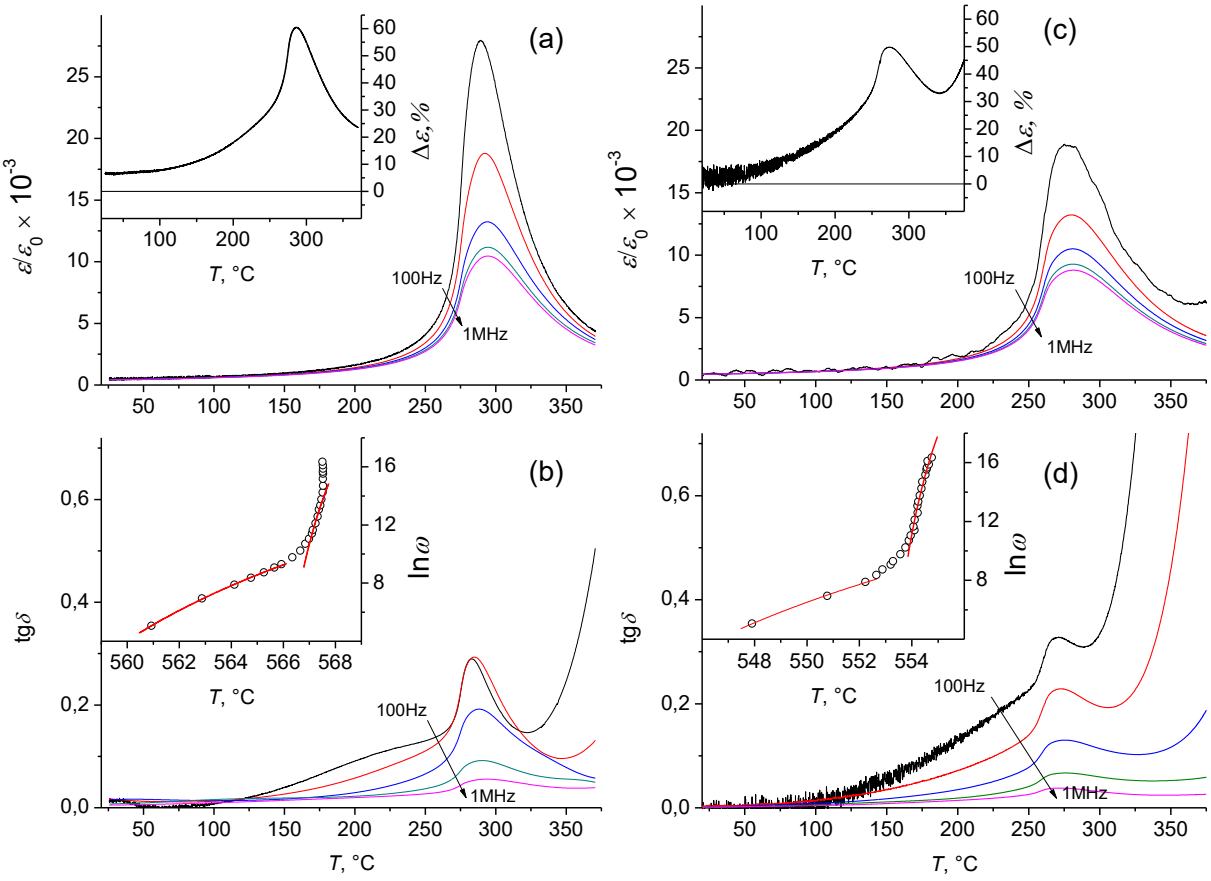

Fig. 3. Dependences of $\varepsilon/\varepsilon_0$ and tanδ of materials SS1 (a,b) and SS2 (c,d) on temperature. The arrows show the direction of temperature change. In the insets of Figures b, d, markers depict the dependences $\ln\omega(T_m)$, where T_m are the temperatures of the maxima $\varepsilon/\varepsilon_0$ obtained at the frequency $\omega = 2\pi f$, and the solid lines illustrate the fulfillment of the Vogel-Fulcher law (3).

Figure 3 shows the dependences of $\varepsilon/\varepsilon_0$ and tgδ of materials SS1 and SS2 on temperature and frequency of the measuring signal. The phase transition (PT) from the ferroelectric to paraelectric state in both materials occurs at similar temperatures: ~294 °C in the case of SS1 and ~281 °C for SS2. Also in both cases there is a strong dispersion of both dielectric constant and dielectric losses. To quantify the depth of dispersion, the parameter $\Delta\varepsilon = 100\% \times (\varepsilon/\varepsilon_{0\ 25Hz} - \varepsilon/\varepsilon_{0\ 1MHz}) / (\varepsilon/\varepsilon_{0\ 1MHz})$ was calculated, the dependences of which on temperature are shown in the insets of Figure 3 a, c. The dispersion $\varepsilon/\varepsilon_0$ begins to increase at temperatures of 100...150 °C and reaches maximum values in the PT region. The dispersion tgδ appears at lower temperatures, and at temperatures above the PT it grows exponentially.

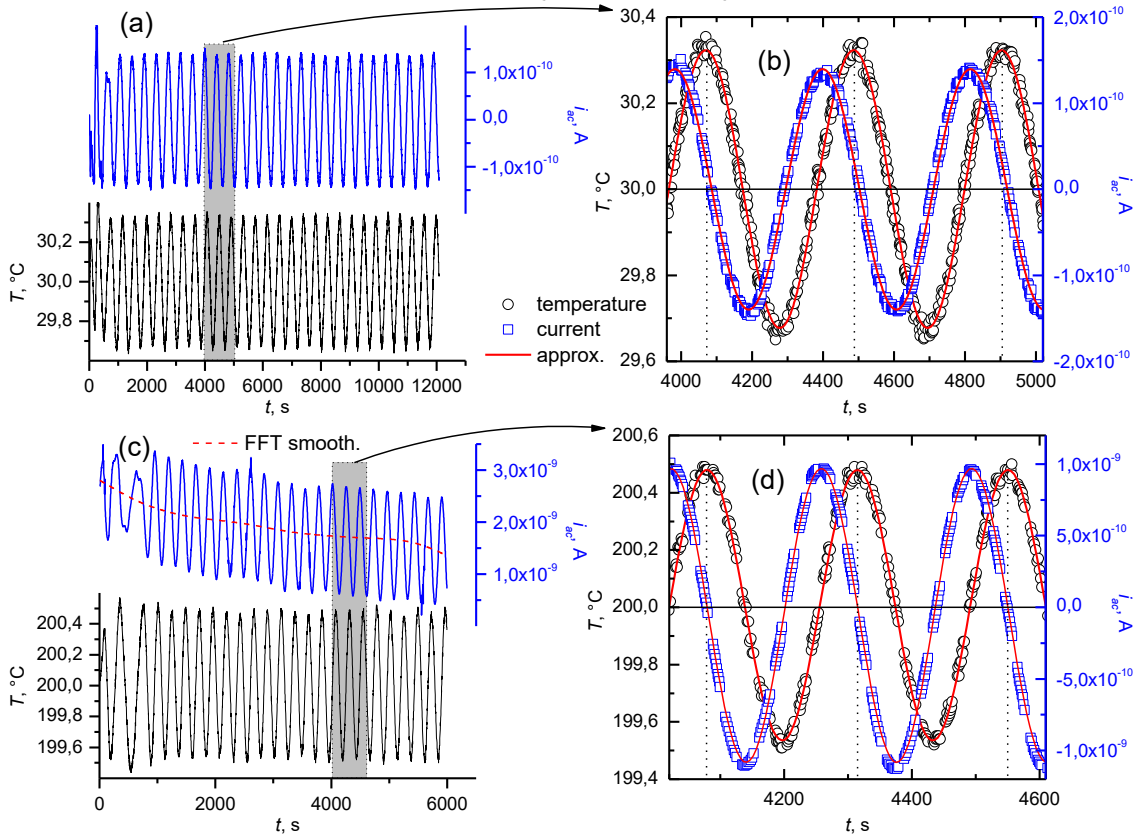

Fig. 4. Time dependences of temperature T and pyroelectric current i for sample SS1, measured at T_0 = 30°C (a, b) and 200°C (c, d). The dotted line in (c) is the result of applying a Fourier filter to the $i(t)$ relationship. The fragments of the dependences $T(t)$ and $i(t)$ shown on the right (b, d) illustrate the correspondence of the temperature wave and the pyroelectric current wave (hollow markers) to expressions (1) and (2) (solid curves).

Figure 4, as an illustration of the application of the temperature wave method, shows the experimental dependences of temperature T and pyroelectric current i on time for sample SS1, measured at T_0 = 30°C (a, b) and 200°C (c, d), as well as the results approximations by expressions (1) and (2), which made it possible to calculate the pyroelectric coefficients p_{HW} given in Table 2. The table also shows the values $\varepsilon^T_{33}/\varepsilon_0$, d_{33}, $|d_{31}|$, as well as the technical coefficients $p_{HW} \times \varepsilon_0 / \varepsilon^T_{33}$ and $p_{HW} / |d_{31}|$, characterizing the detectability and resistance of the pyroelectrics to vibration interference (a decrease in the piezoelectric modulus helps to reduce the piezoelectric polarization that occurs on the electrodes of the pyroelectric under various mechanical influences), respectively.

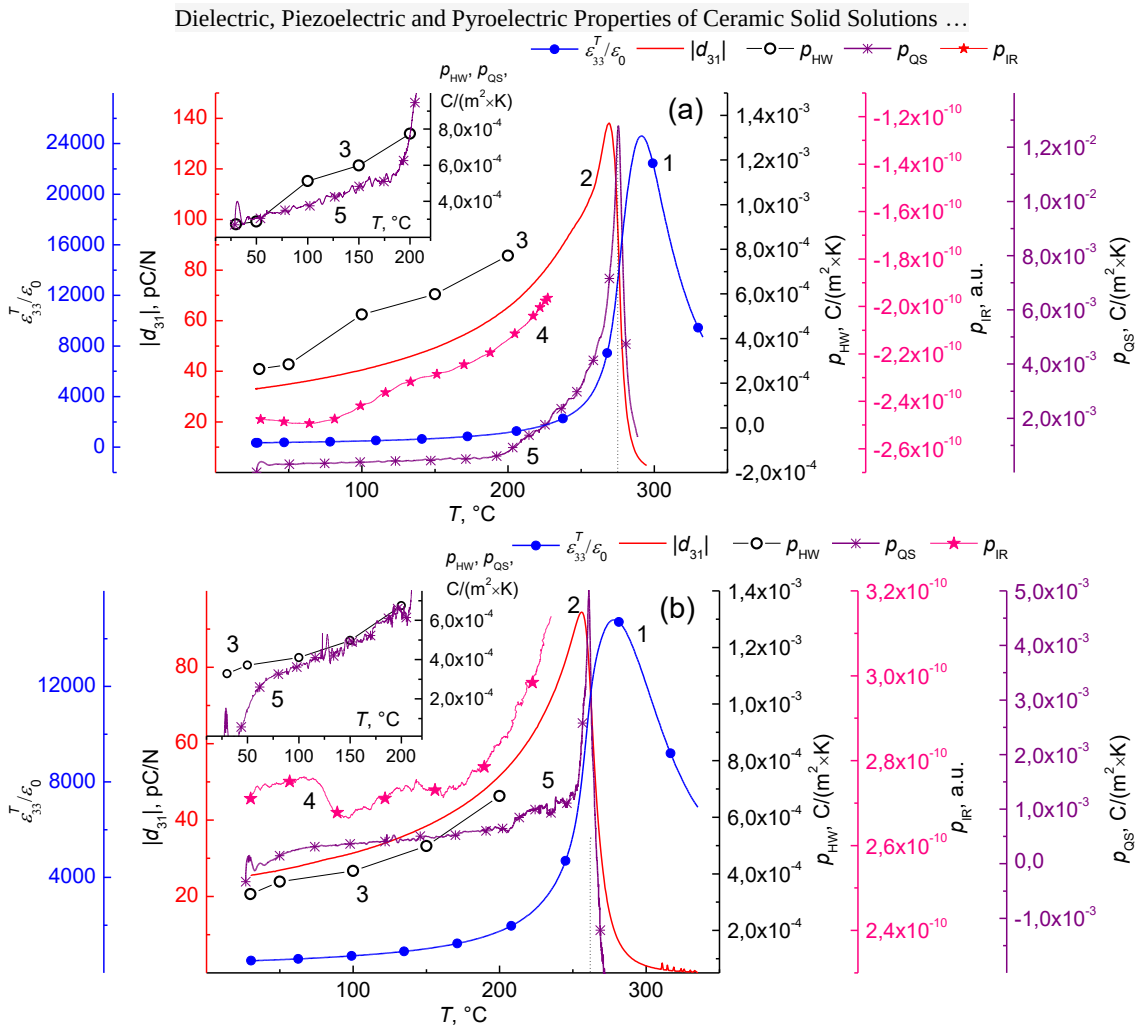

Fig. 5. Dependences of the electrophysical parameters of polarized samples SS1 (a) and SS2 (b): $\varepsilon^T_{33}/\varepsilon_0$ (1), $|d_{31}|$ (2), p_{HW} (3), p_{IR} (4), p_{QS} (5) – depending on temperature.

Table 2. Electrophysical parameters of materials SS1 and SS2, measured at room temperature. For comparison, the parameters of the well-known industrial material PZT-5A are given.

Material	$\varepsilon^T_{33}/\varepsilon_0$	$d_{33} \times 10^{12}$, C/N	$\lvert d_{31}\rvert \times 10^{12}$, C/N	$p_{hw} \times 10^4$, C/(m² × K)	$(p_{hw} \times \varepsilon_0 / (\varepsilon^T_{33} \times C_p) \times 10^6$, C × g/(m² × J)	$(p_{hw} / \lvert d_{31}\rvert) \times 10^{-6}$, N/(m² × K)
SS1	348	118	34	2.6	2.15	7.6
SS2	339	86	25	3.3	3.18	13.2
PZT-5A	1700	374	171	4.7	0.628	2.8

Figure 5 shows the dependences of $\varepsilon^T_{33}/\varepsilon_0$, $|d_{31}|$, p_{HW}, p_{IR} and p_{QS} of polarized samples of materials SS1 and SS2 on temperature. As the phase transition approaches the paraelectric state, the pyroelectric coefficient p_{QS} increases by an order of magnitude, and therefore in the insets it is presented on a scale that makes it possible to compare its values with the results obtained by the temperature wave method.

4 Discussion

Both materials have fairly high T_C and are also characterized by a strong diffusion of the $\varepsilon/\varepsilon_0(T)$ maximum, accompanied by a significant dispersion of the dielectric constant, reaching 60% in the FE PT region. Since X-ray phase analysis did not reveal the presence of impurities with which the observed features could be associated, we carried out a dielectric relaxation analysis according to the method described in [32-34]. This approach made it possible to record shifts in the maxima of the $\varepsilon/\varepsilon_0(T)$ dependences both in the case of SS1 and in the case of SS2, illustrated by the insets in Figure 3c,d, respectively. Here are the dependences of the logarithm of frequency $\omega = 2\pi f$ on the temperature of the maxima (T_m) of the $\varepsilon/\varepsilon_0(T, \omega)$ curves. In both cases, two regions can be distinguished in the $\ln\omega(T_m)$ dependences, differing in different relaxation patterns. The first region (I) – high temperature (high frequency) – is satisfactorily described by the Vogel-Fulcher law:

$$\omega = \omega_0 \exp\left(\frac{E_a}{k(T-T_{VF})}\right), \quad (3)$$

where E_a is the average height of the potential barrier, T is the absolute temperature, k is Boltzmann's constant, ω_0 is the pre-exponential factor and T_{VF} is the "freezing" temperature of the relaxation process. The relaxation width in this region is about one degree; as noted in [35], such weak relaxation can be observed in ferroelectric relaxors in which the characteristic temperature associated with the destruction of the classical domain structure is quite high and close to the T_m region. In the materials under consideration, the relaxor components $PbNb_{2/3}Zn_{1/3}O_3$ and $PbNb_{2/3}Mg_{1/3}O_3$ in the case of SS1 and, apparently, $PbNb_{2/3}Mn_{1/3}O_3$ in the case of SS2, may be responsible for this behavior.

The second, low-temperature region, at first glance, has a classical activation character, however, the Arrhenius law fit gives inadequate activation energy values ($E_a \approx 20$eV), while the application of the Vogel-Fulcher law allows one to obtain more reliable relaxation parameters, the values of which are for both regions and both materials are shown in Table 3. It should be noted that all coefficients were calculated with a large error, which is associated both with the small number of experimental points per region and with the weakness of the described relaxation processes.

Table 3**.** Results of approximation of relaxation processes of the dependences $\varepsilon/\varepsilon_0(T, \omega)$ of ceramics SS1 and SS2 by the Vogel-Fulcher law.

Material	Region	E_a, эВ	ω_0, рад/с	T_{VF}, K
SS1	Region I	$5.54\times10^{-3} \pm 2.44\times10^{-3}$	$6.68\times10^{13} \pm 1.58\times10^{13}$	290.96 ± 0.02
	Region II	$3.56\times10^{-2} \pm 1.36\times10^{-2}$	$1.54\times10^{11} \pm 2.27\times10^{10}$	267.97 ± 3.45
SS2	Region I	$5.09\times10^{-3} \pm 2.32\times10^{-4}$	$1.26\times10^{15} \pm 3.38\times10^{13}$	$278.50 \pm 1.09\times10^{-4}$
	Region II	$4.54\times10^{-2} \pm 1.26\times10^{-3}$	7.20×10^{10}	248.77 ± 0.71

Thus, low-temperature relaxation cannot be associated with Maxwell-Wagner polarization [36], which arises as a result of charge accumulation at grain boundaries, extended defects or pores, which could be expected based on an analysis of the grain structure of the studied ceramics (Figure 2). Most likely, the observed processes are associated with the relaxation of domain walls, the dynamics of which can be "frozen" during their interaction with defects in the crystal structure [37], due to which such relaxation is usually described by the Vogel-Fulcher law with similar

parameters [38]. The contribution of domain walls sandwiched by defects can also explain the observed dispersion of the dielectric constant in the FE PT region, as well as some features of the pyroelectric response of objects.

Firstly, experiments carried out using the temperature wave method revealed some features in the formation of current waves with increasing average temperature. Thus, Figure 4 a, b shows the experimental result, close to the model one: the experimentally measured temperature and current waves are well described by expressions (1) and (2) with parameters T_0 = 30.00 °C, T_1 = 0.32 °C, ω = 0.0151 rad./s, i_{dc} = -1.92×10^{-13} A, i_1 = 1.40×10^{-10} A, ϕ = -1.32 rad. (-75.64°). However, such a correspondence is not always satisfied and in the general case i_{dc} can also depend on time according to some law, which can be observed in Figure 4 c, which shows the dependence $i(t)$ measured at T_0 = 200 °C. In such cases, most often, i_{dc} can be described by an exponential decay function, which indicates the relaxation nature of the observed phenomenon, which can be associated both with temperature activation of free charge carriers and with mechanisms of a different nature, for example, relaxation of domain walls. Since the measurements are carried out in a limited time interval, it is not possible to establish specific parameters of such a dependence, and therefore we processed the experimental data in accordance with the following procedure: the measured current wave was smoothed using a Fourier filter, the smoothed curve represented the dependence of the average value of the wave ($i_{dc}(t)$, dotted line in Figure 4 c), corresponding to the relaxation component of the current, which was subsequently subtracted from the original experimental data. As a result of the subtraction, a purely pyroelectric component remained (Figure 4 d), necessary for calculating the pyroelectric coefficient. In the case of SS1, such a contribution appeared in the measured thermally stimulated current only at T_0 = 200 °C, while in SS2 – already at 100°C, which somehow correlates with the results of the relaxation analysis presented above.

The p_{HW} and p_{QS} coefficients presented in Figure 5 in the case of SS1 in the temperature range of 30...200 °C are in good agreement, while in SS2 in the range of 30...50 °C there is a significant discrepancy in these parameters. This may be due to differences in thermodynamic conditions under which the measurement is carried out. The quasi-static method assumes, albeit slow, but continuous heating of the sample, while in the temperature wave method the temperature stabilizes in the vicinity of T_0 for a long time. As a result, the pyroelectric response can be significantly influenced by the slow relaxation processes of domain walls described above, which in the case of SS2 leads to a significant discrepancy between the pyroelectric coefficients p_{HW} and p_{QS}.

These features of the formation of the dielectric response were reflected in the practically important technical coefficients $p_{HW} \times \varepsilon_0 / \varepsilon^T_{33}$ and $p_{HW} / |d_{31}|$ (Table 2), which at room temperature exceed similar coefficients of known industrial materials, compensating for the initially insufficiently high pyroelectric coefficients of materials SS1 and SS2.

5 Conclusion

Samples of pyroelectric materials based on the $PbZrO_3$-$PbTiO_3$ system: $PbTiO_3$-$PbZrO_3$-$PbNb_{2/3}Zn_{1/3}O_3$-$PbNb_{2/3}Mg_{1/3}O_3$ + MnO_2 (SS1) and $PbTiO_3$-$PbZrO_3$-$PbW_{1/2}Mn_{1/2}O_3$-$PbNb_{2/3}Mn_{1/3}O_3$ (SS2), – were obtained in the form of ceramics using a two-stage solid-phase synthesis followed by mechanical activation of the synthesized powders and sintering using conventional ceramic technology. Analysis of the dielectric spectra of the obtained materials showed that in both cases, the phase transition from the ferroelectric to the paraelectric state is accompanied by a sequence of relaxation processes associated both with the presence of relaxor components in the composition of the objects and with the critical dynamics of domain boundaries interacting with structural defects.

SS2 ceramics have exceptional pyroelectric properties, pyroelectric parameters p_{HW}, $p_{HW} \times \varepsilon_0 / (\varepsilon^T_{33} \times C_p)$ (pyroelectric detectivity) and $p_{HW} / |d_{31}|$ (pyroelectric resistance to vibration interference) at room temperature are 3.3×10^{-4} C/(m^2 × K), 3.18×10^{-6} C × g/(m^2 × J) and 13.2×10^6 N/(m^2 × K), respectively. Such excellent pyroelectric properties are maintained in the temperature range of 30...200°C, which makes this material promising from the point of view of practical applications.

The results of this work can be used in the future in the development of pyroelectric detectors used for remote measurement of the temperature of heated bodies, including moving ones (rolling mills, high-frequency furnaces for hardening or tempering steel; plastic production; food industry, etc.); for measuring power systems; control of overheating of rubbing parts, etc.); in protection systems (from fire, from intruders), which determines the relevance and significance of the results obtained in the work.

Acknowledgements

The study was supported by a grant from the Russian Science Foundation № 23-12-00351, https://rscf.ru/project/23-12-00351/

References

1. Mason WP. Piezoelectricity, its history and applications// J Acoust Soc Am. 1981. V.70. P. 1561–6.
2. Karapuzha AS, James NK, Khanbareh H, van der Zwaag S, Groen WA. Structure, dielectric and piezoelectric properties of donor doped PZT ceramics across the phase diagram// Ferroelectrics. 2016. V.504. P. 160–71.
3. Boucher E, Guiffard B, Lebrun L, Guyomar D. Effects of Zr/Ti ratio on structural, dielectric and piezoelectric properties of Mn-and (Mn, F)-doped lead zirconate titanate ceramics// Ceram Int. 2006. V. 32. P.479–85.
4. Zachariasz R, Bochenek D. Properties of the PZT type ceramics admixed with barium and niobium// Arch Metall Mater. 2009. V. 54. P. 895–902.
5. Raevski IP, Kuprina YA, Zakharchenko IN, Gusev AA, Isupov VP, Bunina OA, Titov VV, Raevskaya SI, Malitskaya MA, Blazhevich AV, Orlov SV, Sitalo EI. Structural and dielectric studies of $PbYb_{1/2}Nb_{1/2}O_3$ ceramics with the differing degree of the long-range compositional ordering fabricated by mechanoactivation. In: Parinov IA, et al., editors. Advanced materials, Springer proceedings in physics, vol. 207. Berlin: Springer; 2018. p. 209–24.
6. Xiang P-H, Dong X-L, Chen H, Zhang Z, Guo J-K. Mechanical and electrical properties of small amount of oxides reinforced PZT ceramics// Ceram Int. 2003. V.29. P.499–503.
7. Li J, Sun Q. Effects of Cr_2O_3 doping on the electrical properties and the temperature stabilities of PZT binary piezoelectric ceramics// Rare Met. 2008. V.27. P.362–6.
8. Bedoya C, Muller C, Baudour J-L, Madigou V, Anne M, Roubin M. Sr-doped $PbZr_{1-x}Ti_xO_3$ ceramic: structural study and field-induced reorientation of ferroelectric domains// Mater Sci Eng B. 2000. V.75. P.43–52.
9. Gao F, Cheng L-H, Hong R-Z, Liu J, Wang C-J, Tian C. Crystal structure and piezoelectric properties of $x Pb(Mn_{1/3}Nb_{2/3})O_3$–$(0.2-x)Pb(Zn_{1/3}Nb_{2/3})O_3$–$0.8Pb(Zr_{0.52}Ti_{0.48})O_3$ ceramics// Ceram Int. 2009. V.35. P. 1719–23.
10. Yimnirun R, Ananta S, Laoratanakul P. Effects of $Pb(Mg_{1/3}Nb_{2/3})O_3$ mixed-oxide modification on dielectric properties of $Pb(Zr_{0.52}Ti_{0.48})O_3$ ceramics// Mater Sci Eng B. 2004. V.112. P.79–86.

11. Prasatkhetragarn A, Yimnirun R. Phase formation, electrical properties and morphotropic phase boundary of $0.95Pb(Zr_xTi_{1-x})O_3–0.05Pb(Mn_{1/3}Nb_{2/3})O_3$ ceramics// Ceram Int. 2013. V.39. P. S91–5.
12. Andryushina I.N., et al. The PZT system ($PbZr_{1-x}Ti_xO_3$, $0.0\leq x\leq 1.0$): specific features of recrystallization sintering and microstructures of solid solutions (Part 1) // Ceramics International. 2013. V. 39. P. 753.
13. Andryushina I.N., et al. The PZT system ($PbTi_xZr_{1-x}O_3$, $0\leq x\leq 1.0$): The real phase diagram of solid solutions (room temperature) (Part 2) // Ceramics International. 2013. V. 39. P. 1285.
14. Andryushina I.N., et al. The PZT system ($PbTi_xZr_{1-x}O_3$, $0\leq x\leq 1.0$): High temperature X-ray diffraction studies. Complete x–T phase diagram of real solid solutions (Part 3) // Ceramics International. 2013. V. 39. P. 2889.
15. Andryushina I. N., et al. Crystal structure, microstructure and electrophysical properties of highly sensitive ferroactive materials based on the $Pb(Zr_{1-x}Ti_x)O_3$ system // Materials Science and Engineering: B. 2022. V. 283. P. 115804.
16. Pavelko A., Shilkina L., Reznichenko L. Phase states and electrophysical properties of multicomponent perovskite solid solutions on the base of PMN-PT and PZT systems // Journal of Advanced Dielectrics. 2020. Vol. 10. No 1-2. Art. № 2060011 (6 p.).
17. Pavelko A. A. Piezodielectric properties of PMN–PZT–PT solid solutions under the action of high temperatures // Bulletin of the Russian Academy of Sciences: Physics. 2014. Vol. 78. No 8. P. 802-803.
18. Zakharov Y.N., Raevskaya S.I., Lutokhin A.G., Titov V.V., Raevski I.P., Smotrakov V.G., Eremkin V.V., Emelyanov A.S., Pavelko A.A. Field-induced enhancement of pyroelectric response of $PbMg_{1/3}Nb_{2/3}O_3$-$PbTiO_3$ and $PbFe_{1/2}Nb_{1/2}O_3$-$PbTiO_3$ solid solution ceramics // Ferroelectrics. 2010. Vol. 399. № 1. P. 20-26.
19. 1Andryushina, I.N., et al.: The PZT system ($PbZr_{1-x}Ti_xO_3$, $0.0\leq x\leq 1.0$): specific features of recrystallization sintering and microstructures of solid solutions (Part 1). Ceramics International 39, 753 (2013).
20. Andryushina, I.N., et al.: The PZT system ($PbTi_xZr_{1-x}O_3$, $0\leq x\leq 1.0$): The real phase diagram of solid solutions (room temperature) (Part 2). Ceramics International 39, 1285 (2013).
21. Andryushina, I.N., et al.: The PZT system ($PbTi_xZr_{1-x}O_3$, $0\leq x\leq 1.0$): High temperature X-ray diffraction studies. Complete x–T phase diagram of real solid solutions (Part 3). Ceramics International 39, 2889 (2013).
22. Andryushina, I. N., et al.: Crystal structure, microstructure and electrophysical properties of highly sensitive ferroactive materials based on the $Pb(Zr_{1-x}Ti_x)O_3$ system Materials Science and Engineering: B 283, 115804 (2022).
23. Pavelko, A., Shilkina, L., Reznichenko, L.: Phase states and electrophysical properties of multicomponent perovskite solid solutions on the base of PMN-PT and PZT systems. Journal of Advanced Dielectrics 10. Art. № 2060011 (2020).
24. Pavelko, A.A.: Piezodielectric properties of PMN–PZT–PT solid solutions under the action of high temperatures. Bulletin of the Russian Academy of Sciences: Physics 78, 802-803 (2014).
25. Zakharov, Y.N., et.al.: Field-induced enhancement of pyroelectric response of $PbMg_{1/3}Nb_{2/3}O_3$-$PbTiO_3$ and $PbFe_{1/2}Nb_{1/2}O_3$-$PbTiO_3$ solid solution ceramics. Ferroelectrics 399, 20-26 (2010).
26. 8Fesenko, E.G., Danziger, A.Ya., Razumovskaya, O.N.: New piezoceramic materials. Rostov-on-Don. Publishing house of the Russian State University. 156 p. (1983) [in Russian].
27. IEEE Standard on Piezoelectricity ANSI/IEEE Std 176-1987, New-York, 1988. DOI: 10.1109/IEEESTD.1988.79638.

28. Whatmore, R.: Characterisation of pyroelectric materials. Characterisation of ferroelectric bulk materials and thin films. Dordrecht: Springer Netherlands, 2014. P. 65-86.
29. Garn, L.E., Sharp, E.J.: Use of low-frequency sinusoidal temperature waves to separate pyroelectric currents from nonpyroelectric currents. Part I. Theory. J. Appl. Phys. 53, 8974–8979 (1982).
30. Garn, L.E., Sharp, E.J.: Use of low-frequency sinusoidal temperature waves to separate pyroelectric currents from nonpyroelectric currents. Part II. Experiment. J. Appl. Phys. 53, 8980–8987 (1982).
31. Chynoweth, A.G.: Dynamic method for measuring the pyroelectric effect with special reference to barium titanate. J. Appl. Phys. 27, 78 (1956).
32. Pavelko, A.A.: Effect of Li_2CO_3 modification on the formation of the ferroelectric properties of $PbFe_{0.5}Nb_{0.5}O_3$ ceramic targets and thin films prepared by RF cathode sputtering. Journal of Alloys and Compounds 836, Art. № 155371 (2020).
33. Pavelko, A.A., Pavlenko, A.V., Reznichenko, L.A.: Effect of lithium carbonate modification on the ferroelectric phase transition diffusion in lead ferroniobate ceramics. Journal of Advanced Dielectrics 12, 2160021 (2022).
34. Talanov, M.V., Pavelko, A.A., Kamzina, L.S.: Domain-wall freezing in $Cd_2Nb_2O_7$ pyrochlore single crystal. Materials Research Bulletin 145, 111548 (2022).
35. Li, F., et.al.: Local Structural Heterogeneity and Electromechanical Responses of Ferroelectrics: Learning from Relaxor Ferroelectrics. Advanced Functional Materials 28, 1801504 (2018).
36. Turik, A.V., Radchenko, G.S.: Maxwell-Wagner relaxation in piezoactive media. Journal of Physics D: Applied Physics 35, 1188 (2002).
37. Tagantsev, A.K., Cross, L.E., Fousek, J.: Domains in Ferroic Crystals and Thin Films. Springer- New York, 2010.
38. Huang, Y.N., Li, X., Ding, Y., Wang, Y.N., Shen, H.M., Zhang, Z.F., Fang, C.S., Zhuo, S.H., Fung, P.C.W.: Domain freezing in potassium dihydrogen phosphate, triglycine sulfate, and CuAlZnNi. Phys. Rev. B: Condens. Matter Mater. Phys. 55, 16159-16167 (1997).

Cover letter

Dear editor!

Please find an article «Dielectric, Piezoelectric and Pyroelectric Properties of Ceramic Solid Solutions Based on PMN-PT and PZT» of the authors: Aleksey Pavelko, Alexander Martynenko, Konstantin Andryushin, Ekaterina Glazunova, Alexander Nagaenko, Lidiya Shilkina, Suleiman Kallaev, Larisa Reznichenko.

The article describes the results of the creation and research of ceramic solid solutions based on PZT and PMN-PT systems. The formation patterns of their crystalline structure, microstructure and electrophysical properties in a wide range of temperatures were studied. The objects studied were found to possess fairly high Curie temperatures and pyroelectric coefficients, high coefficients of pyroelectric sensitivity and resistance to vibration interference, which makes it possible to classify them as pyroelectric materials promising for use as working elements of sensors for pyroelectric receivers of radiant (thermal) energy.

The article is original and unpublished and is not being or having been submitted for publication to any other journal. All the authors have read the paper and agree with its submission to Materials Research Express.

On behalf of the authors

A.A. Pavelko

Declaration of interests

☐The authors declare that they have no known competing financial interests or personal relationships that could have appeared to influence the work reported in this paper.

☒The authors declare the following financial interests/personal relationships which may be considered as potential competing interests:

Aleksey Pavelko reports financial support was provided by Russian Science Foundation. Aleksey Pavelko reports a relationship with Russian Science Foundation that includes: funding grants. If there are other authors, they declare that they have no known competing financial interests or personal relationships that could have appeared to influence the work reported in this paper.

Figure 1a

Click here to access/download;Figure;fig1a.eps

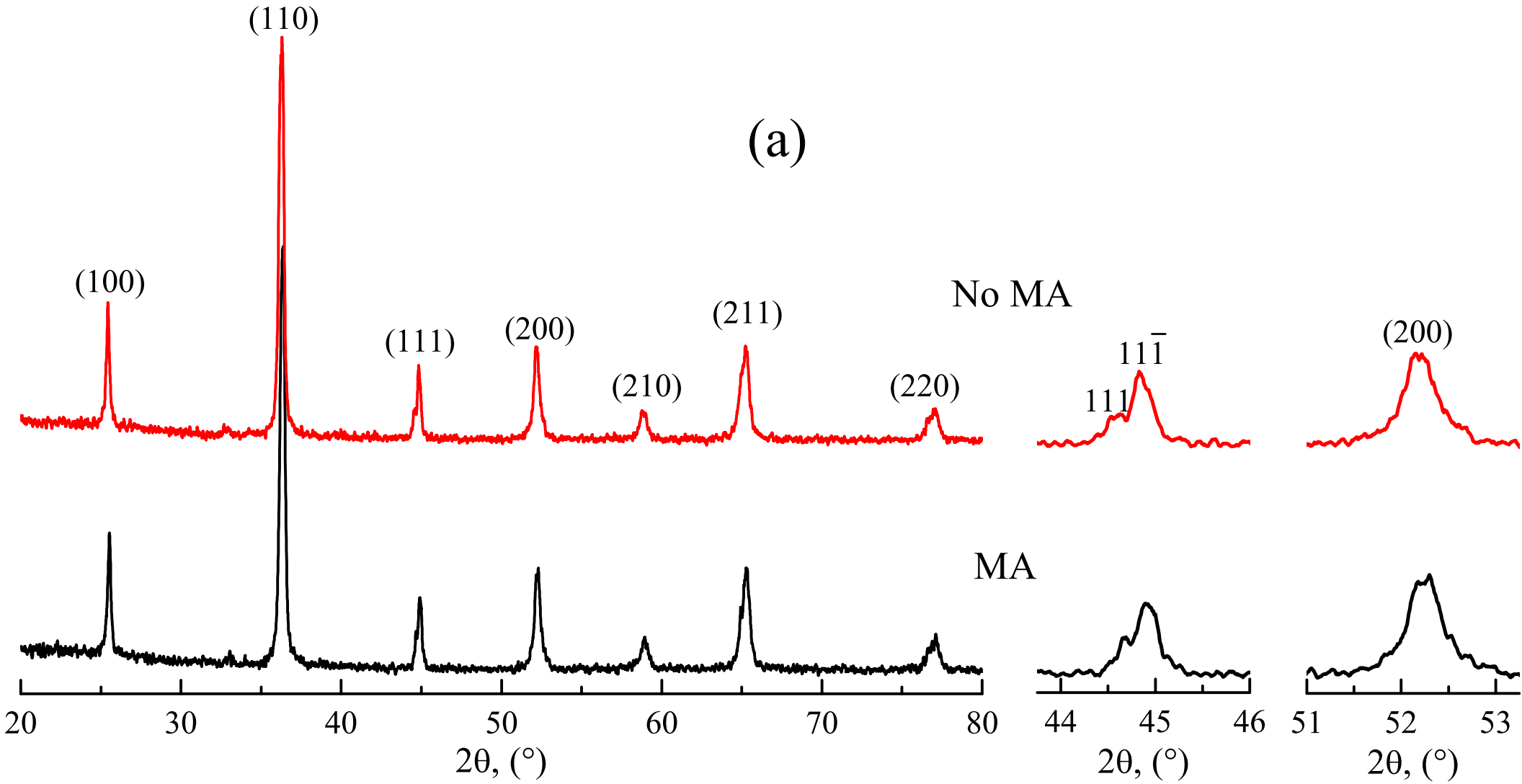

Figure 1b

Click here to access/download;Figure;fig1b.eps

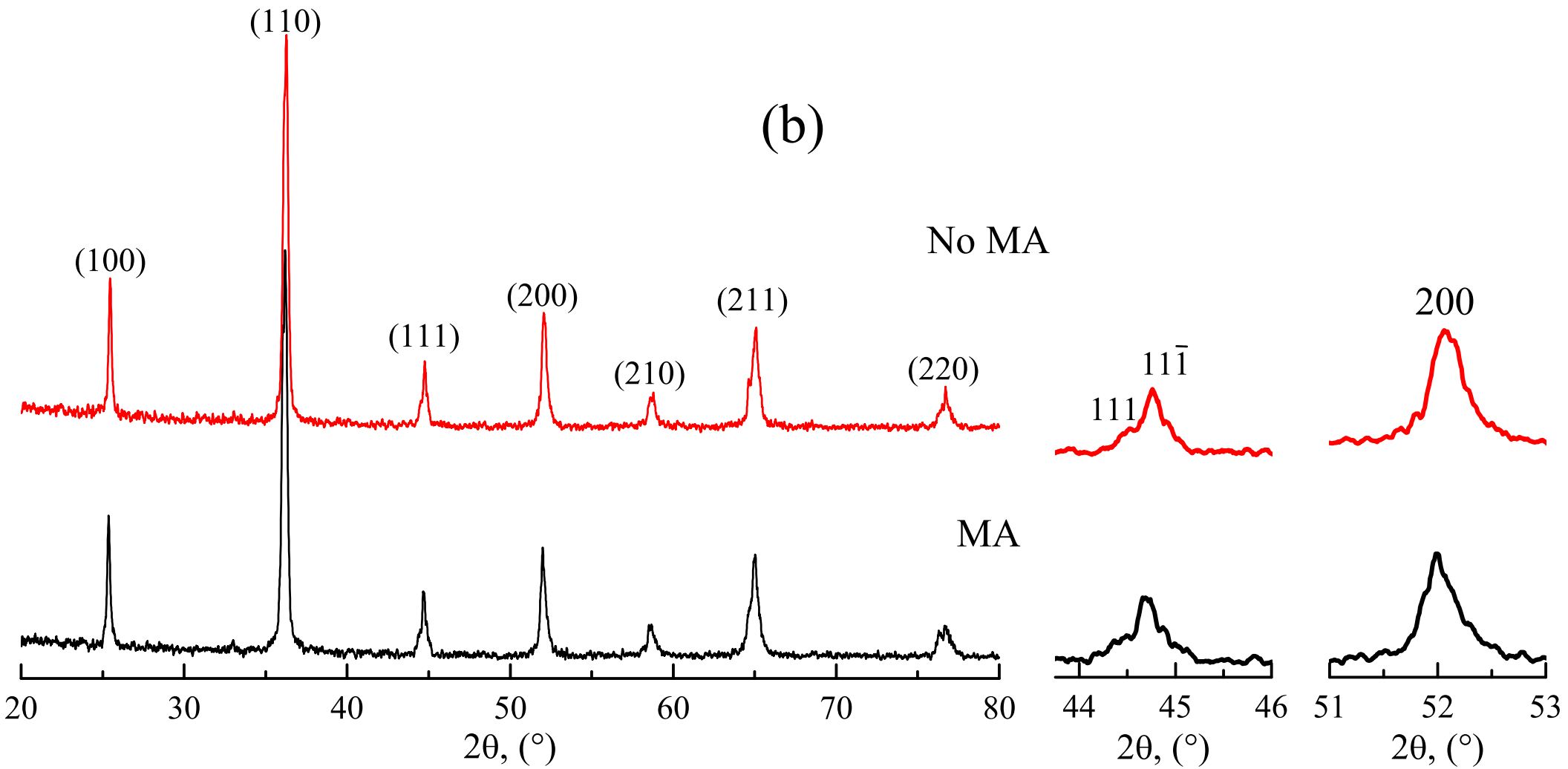

Figure 2a

Click here to access/download;Figure;fig2a.jpg

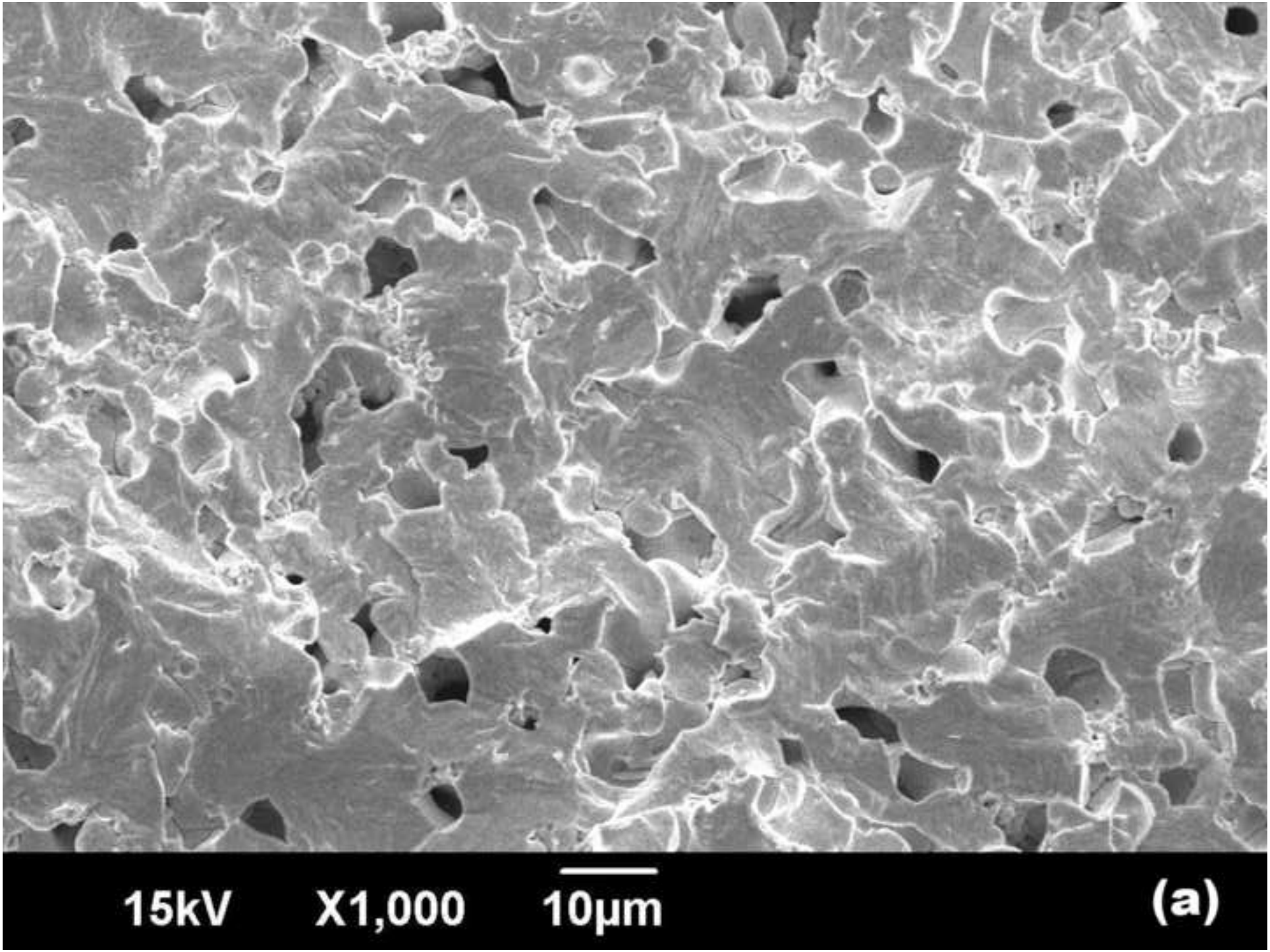

Figure 2b

Click here to access/download;Figure;fig2b.jpg

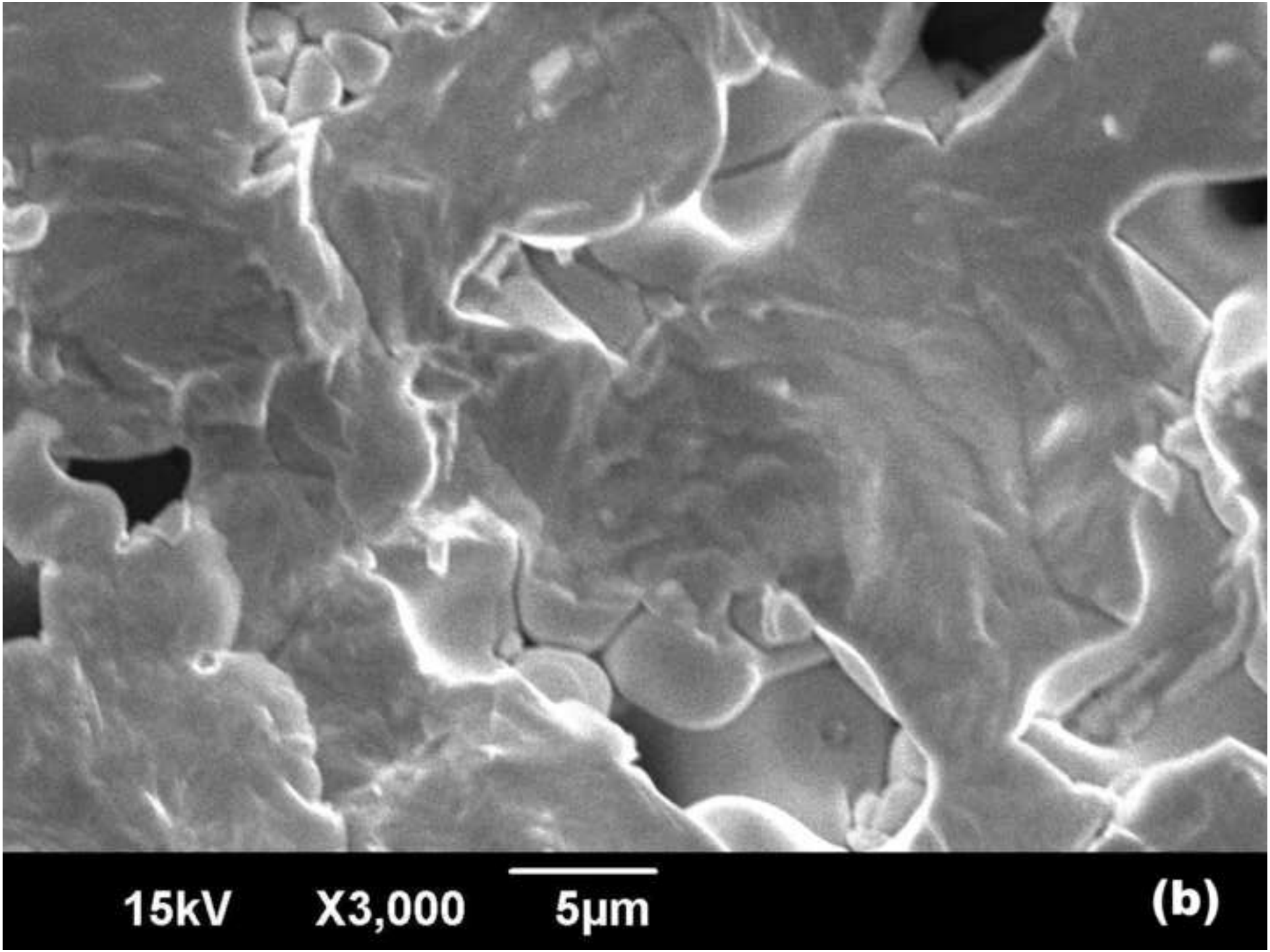

Figure 2c

Click here to access/download;Figure;fig2c.jpg

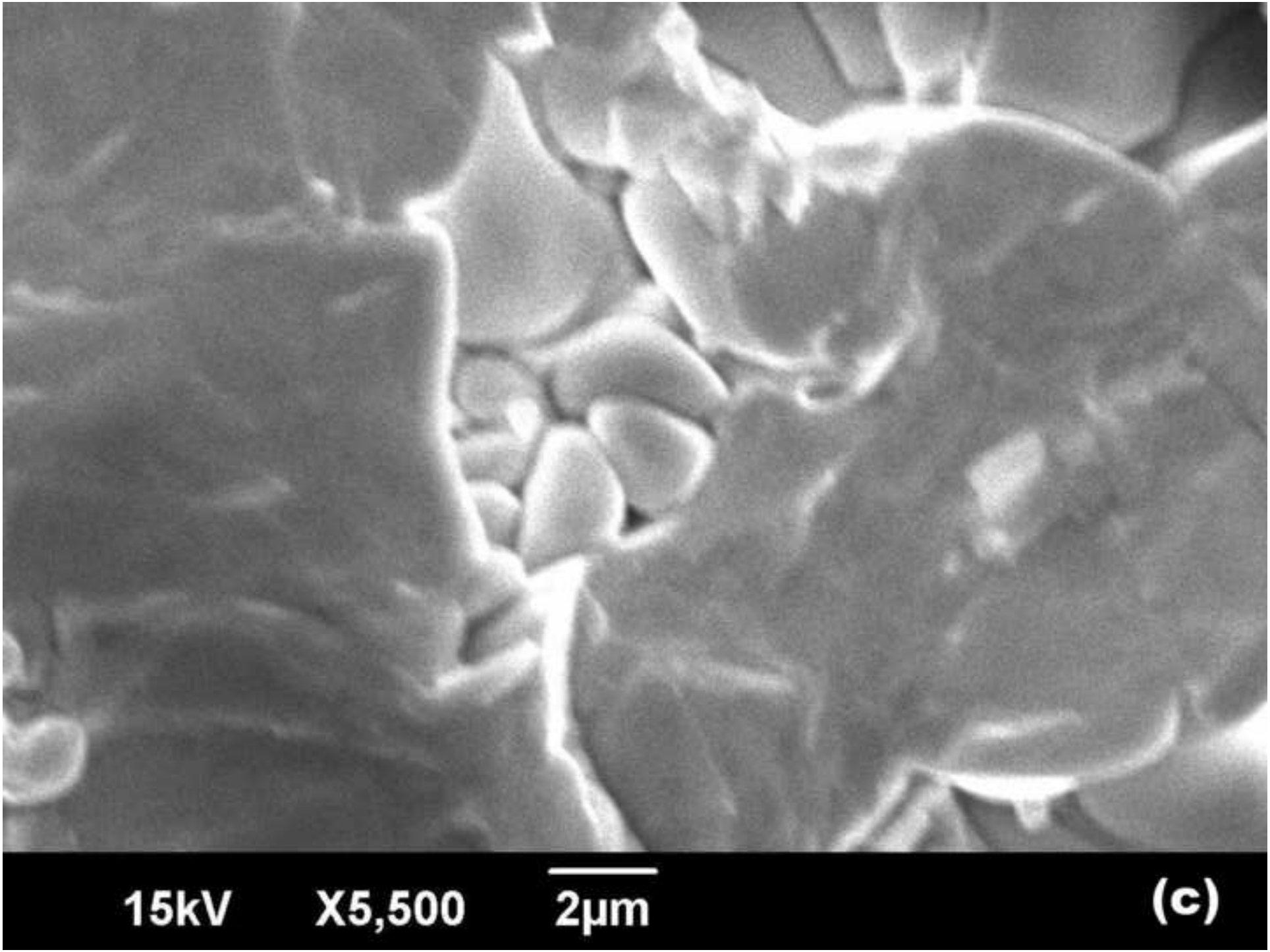

Figure 2d

Click here to access/download;Figure;fig2d.jpg

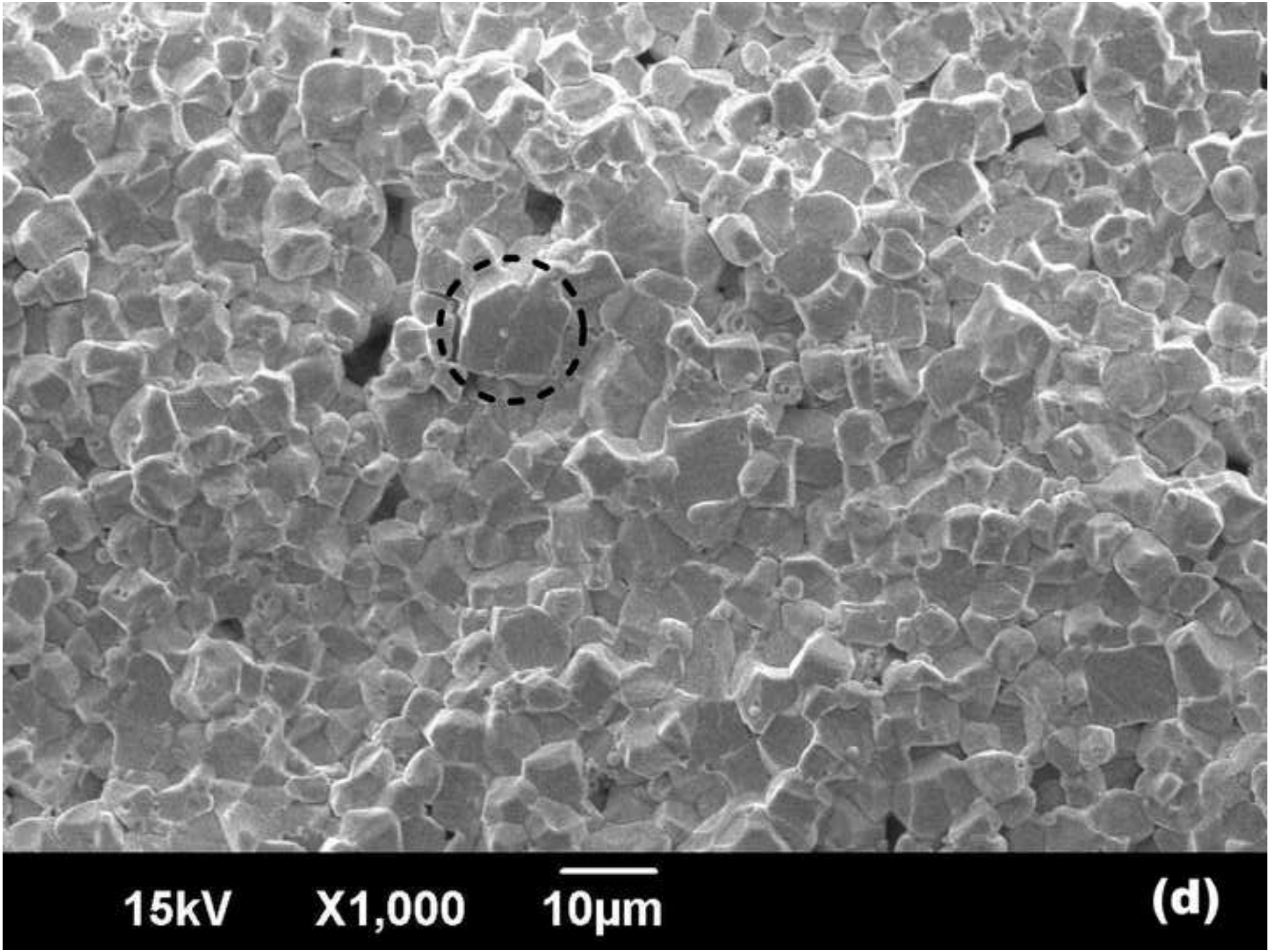

Figure 2e

Click here to access/download;Figure;fig2e.jpg

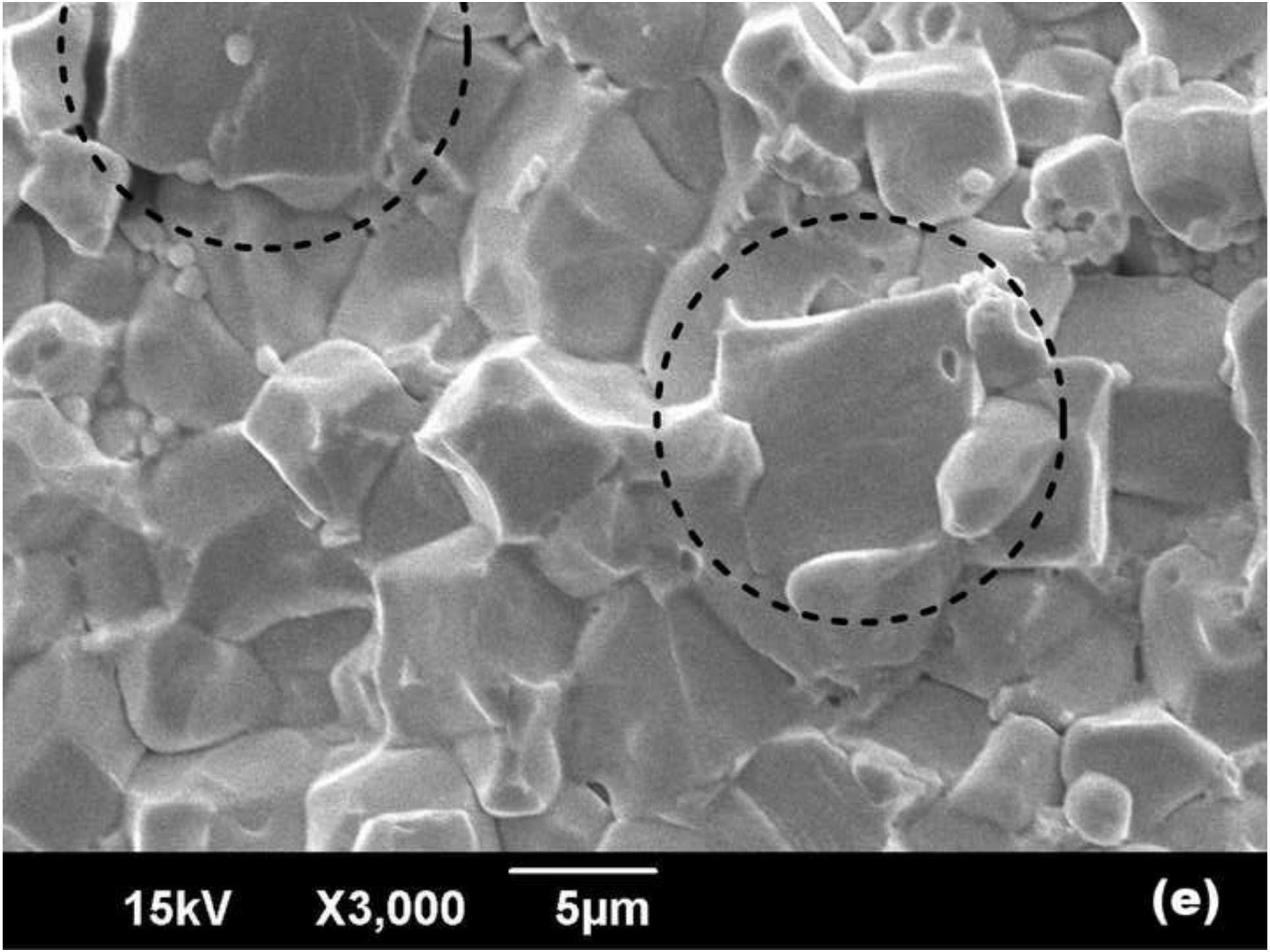

Figure 2f

Click here to access/download;Figure;fig2f.jpg

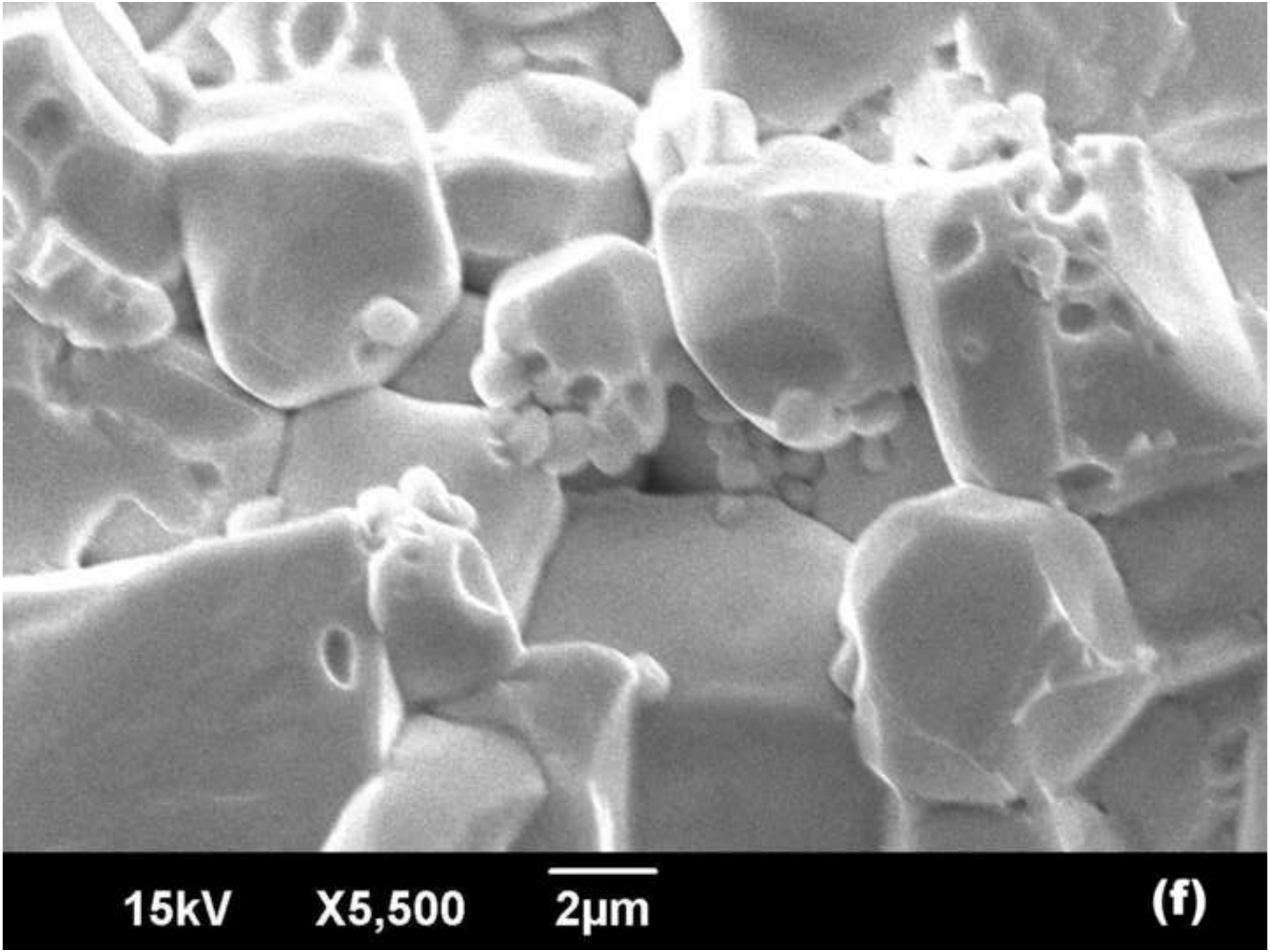

Figure 3ab

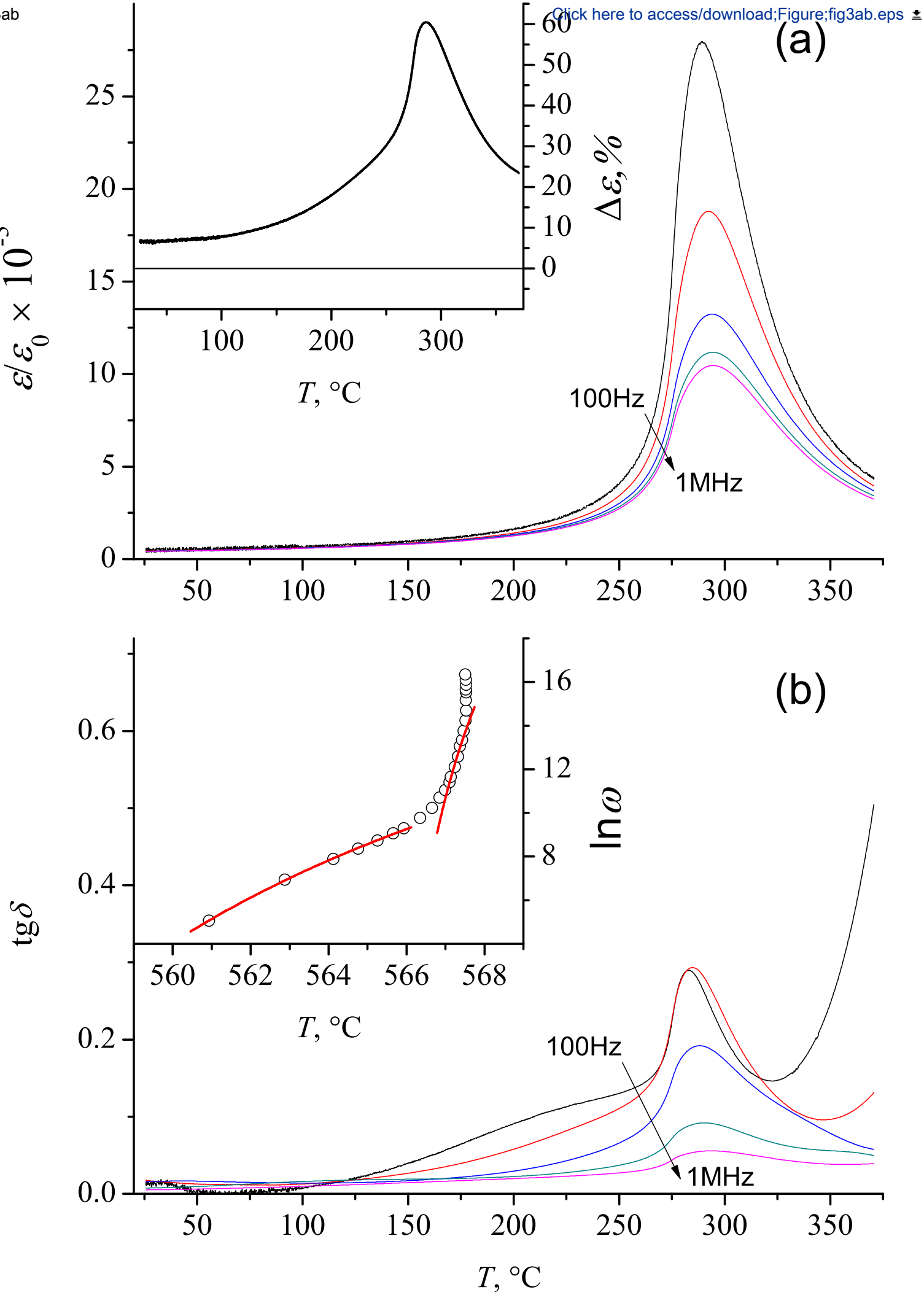

Figure 3cd

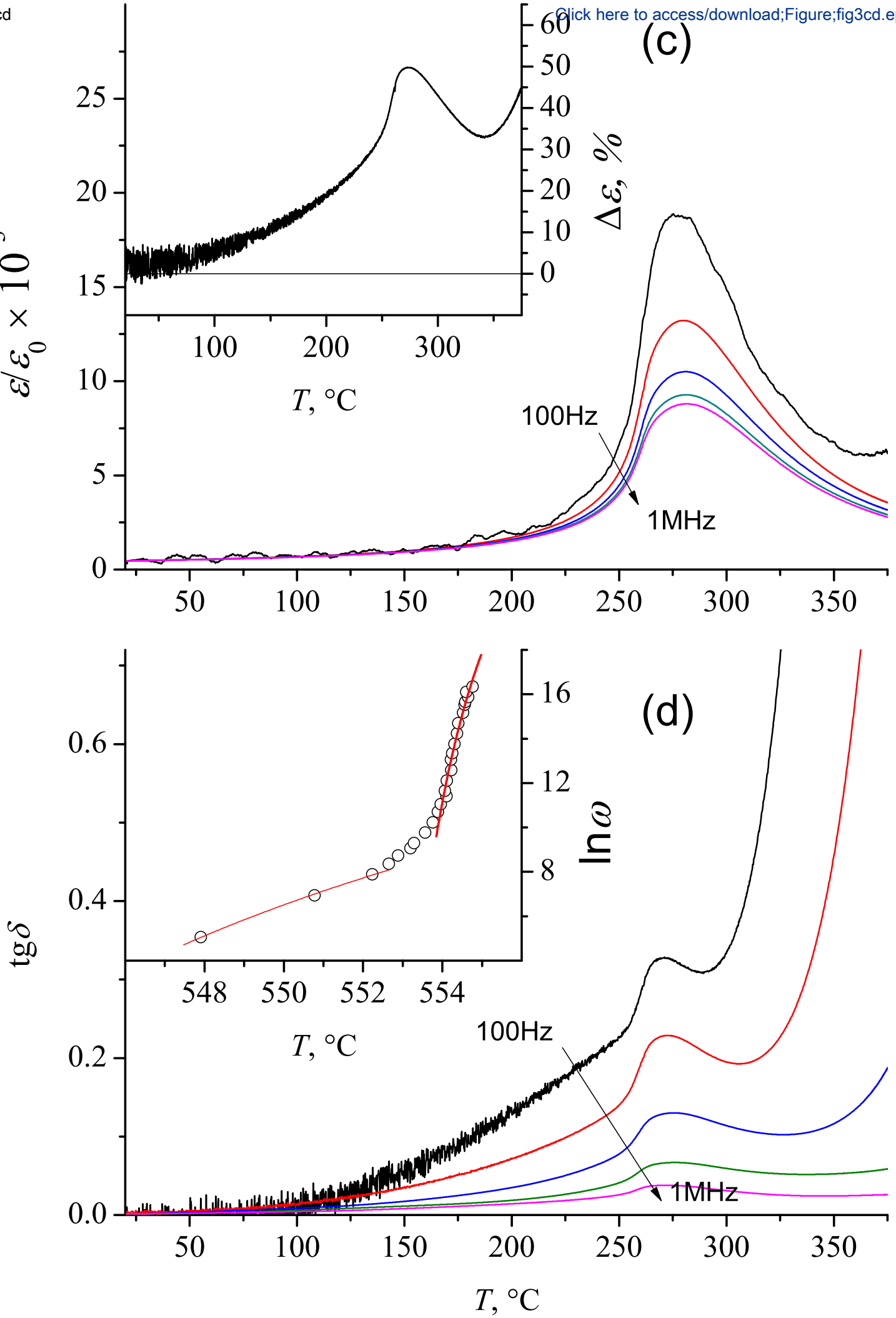

Figure 4ab

Click here to access/download;Figure;fig4ab.eps

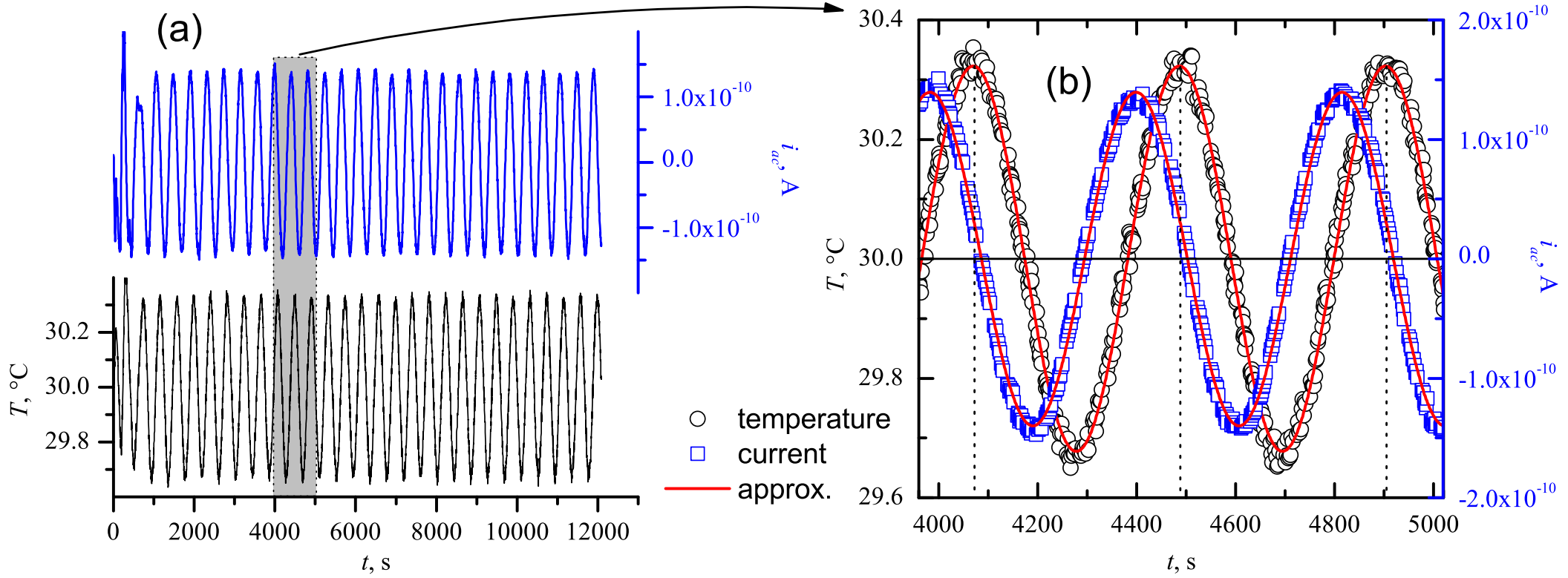

Figure 4cd

Click here to access/download;Figure;fig4cd.eps

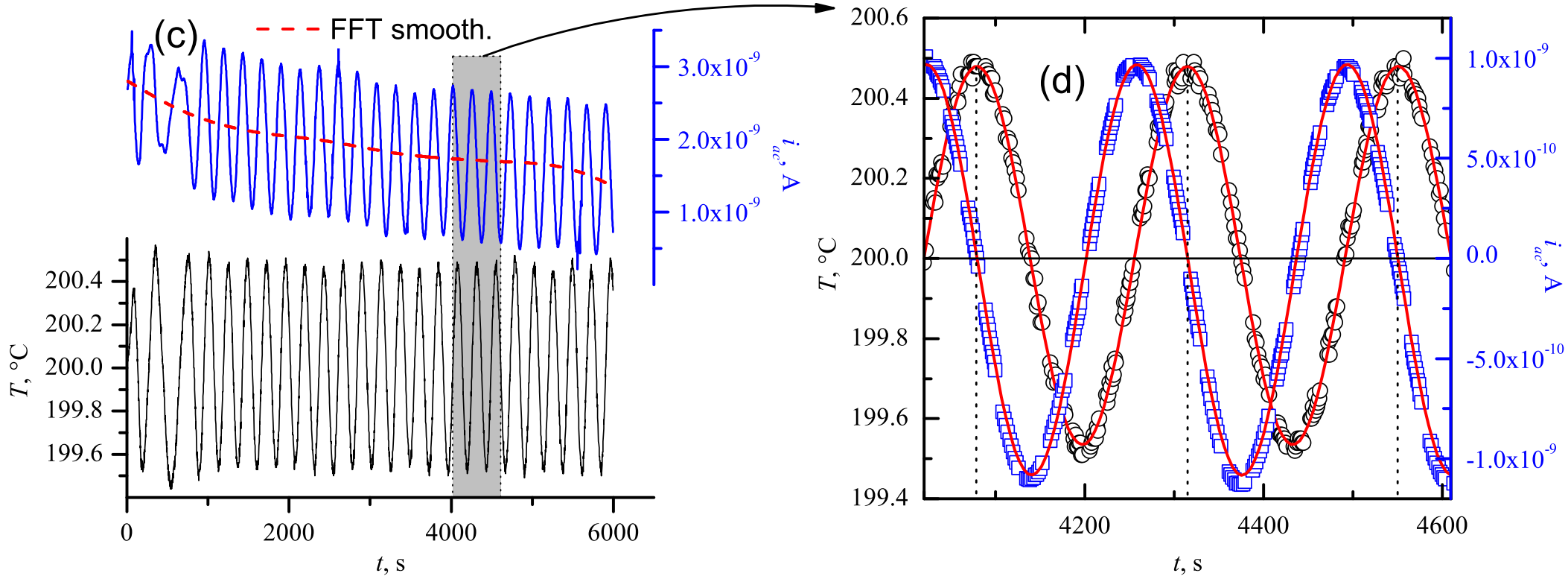

Figure 5a

Click here to access/download;Figure;fig5a.eps

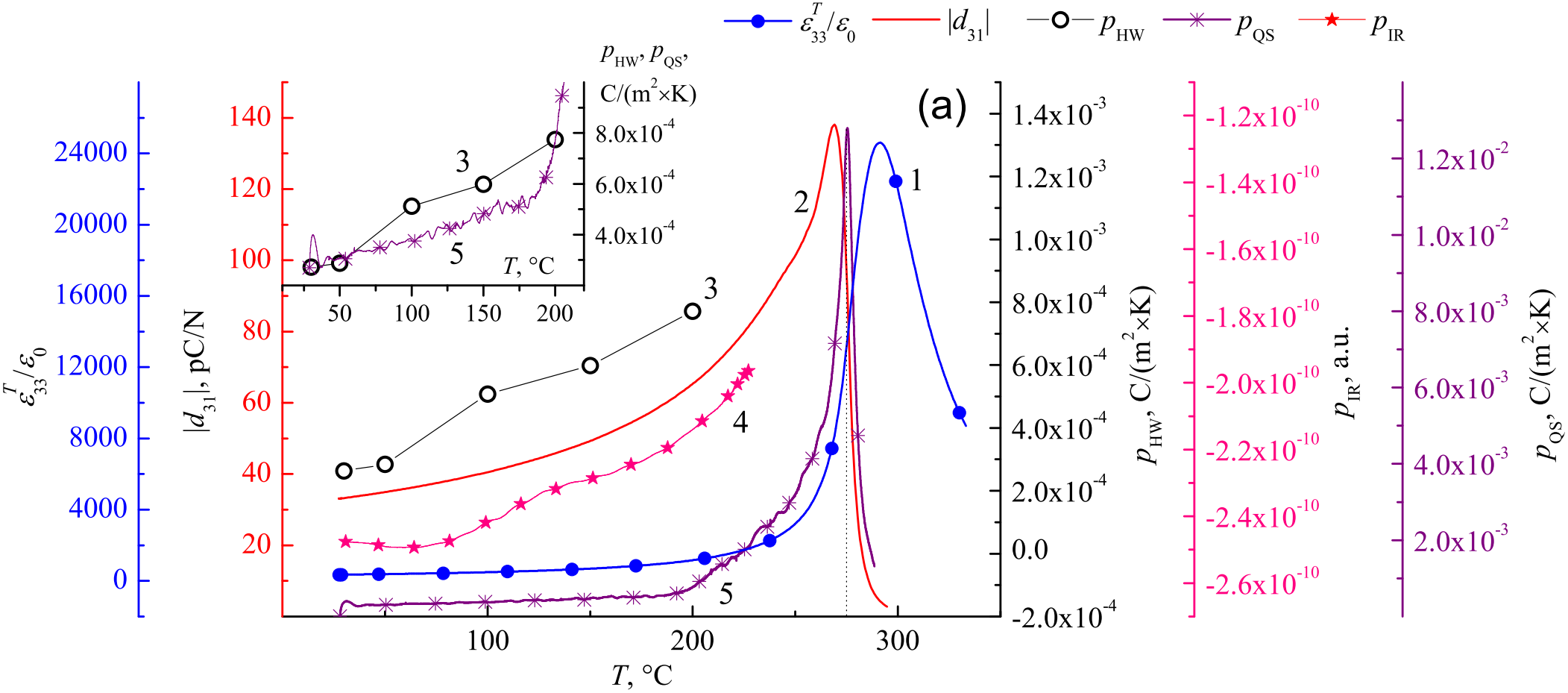

Figure 5b

Click here to access/download;Figure;fig5b.eps